Chitosan-Derived Iron Oxide Systems for Magnetically Guided and Efficient Water Purification Processes from Polycyclic Aromatic Hydrocarbons

Chitosan-derived Iron Oxide Systems for Magnetically Guided and Efficient Water Purification Processes from Polycyclic Aromatic Hydrocarbons

Roberto Nisticò[a,‡], Flavia Franzoso[a,‡], Federico Cesano[a,b], Domenica Scarano[a,b], Giuliana Magnacca[a,b], Maria E. Parolo[c] and Luciano Carlos[d,*].

[a] University of Torino, Department of Chemistry, and [b] NIS (Nanostructured Interphases and Surfaces) Centre, Via P. Giuria 7, 10125 Torino, Italy.

[c] Instituto de Investigación en Toxicología Ambiental y Agrobiotecnología, CITAAC (CONICET-UNCo), Facultad de Ingeniería, Universidad Nacional Del Comahue, Buenos Aires 1400, Neuquén, Argentina.

[d] Instituto de Investigación y Desarrollo en Ingeniería de Procesos, Biotecnología y Energías Alternativas, PROBIEN (CONICET-UNCo), Buenos Aires 1400, Neuquén, Argentina.

‡ Both authors contributed equally to this work.

* Corresponding author. E-mail: luciano.carlos@probien.gob.ar, Phone.: +54 299 4490300, Postal address: Buenos Aires 1400 (CP 8300), Neuquén, Argentina.

Abstract

Chitosan and pyrolyzed chitosan, acting as protective frameworks of magnetic nanoparticles (magnetite/maghemite and/or metallic Fe) have been investigated to be used in magnetically-guided water remediation processes from polycyclic aromatic hydrocarbons (PAHs). Chitosan-derived magnet-sensitive materials were first obtained by a one-step co-precipitation method, then two carbon-derived magnetic chitosan materials were obtained under N_2 gas flow at 550°C and 800°C, respectively. The obtained materials were investigated by means of X-ray diffraction (XRD), FTIR spectroscopy, Scanning Electron Microscopy (SEM), High Resolution Transmission Electron Microscopy (HRTEM), Atomic Force Microscopy (AFM), Magnetic Force Microscopy (MFM), and magnetization measurements. Thermal treatment conditions, along with the amounts of chitosan used in the synthesis processes, played a critical role in the crystal structure and magnetic properties of the obtained nanomaterials. The adsorption capacity of chitosan-derived magnet-sensitive materials was tested towards PAHs. The results indicate high sorption capacity for anthracene and naphthalene onto the chitosan-derived material pyrolyzed at 550°C. Furthermore, experiments performed with a mixture of eight PAHs show that PAH molecules with higher hydrophobicity and more extended aromaticity had stronger sorption capacity. Interestingly, due to the obtained results, the use of chitosan is encouraged as a platform for the creation of green adsorbents for further developments in wastewater purification treatments.

Keywords: Carbon coating; Chitosan; Iron oxides; Magnetic materials; PAHs adsorption; Pyrolysis.

Introduction

Since the beginning of the 20th century, due to rapid industrial development, the hydrophobic organic pollution of the marine environment is one of the main ecological issues [1-3]. In fact, significant amounts of polycyclic aromatic hydrocarbons (PAHs) have been released to the environment by anthropogenic activities, including military operations, vehicular emissions, agricultural production, residential waste burning, combustion of fossil fuels, leakage from the petroleum industry, manufacturing of carbon black, coal tar pitch and asphalt, heating and power generation, and emissions from internal combustion engines [4-5]. As for polycyclic aromatic hydrocarbons, due to their hydrophobic nature and chemical resistance, it is known they are persistent compounds having harmful effects on human health, wildlife and biological diversity. According to this, the selection of a suitable clean-up technique for PAHs, as well as the effectiveness of the remediation procedure on the surrounding environment is mandatory [6-8]. Recent works have shown that the most used techniques for water remediation from hydrocarbons pollution are based on: i) physical (by using booms, skimmers, and adsorbents), ii) chemical (photocatalysis or by using dispersants and solidifiers), iii) thermal (i.e. *in situ* burning), and iv) biological (i.e. bioremediation) processes [9]. A comprehensive review on the different remediation approaches is out of the scope of this manuscript and can be found elsewhere [4,9-12]. To the best of our knowledge and limited to physical methods, the simplest process which can be used both in open-space polluted areas as well as in wastewater treatment plants is the physical remediation by means of adsorbents. Conventional adsorbents can be either synthetic or natural (in)organic in nature. Among the main synthetic sorbents (the most used), polymeric (polypropylene, polystyrene, polyester, and polyurethane) foams and activated carbons are preferred for their surface properties (porosity and hydrophobicity) [9,13-14]. As far as the natural sorbents are concerned, bio-derived products, with low cost source and environmental-friendly nature, have received a growing interest. Among these, chitosan is an amino polysaccharide derived from very abundant chitin (component of crabs, lobster and shrimps shells, squid and octopus radulae, beaks and cuttlebones, cuticles of insects and cell walls of some fungi) [15-17]. Due to their chemical structure and physicochemical properties [18-20], chitosan and related systems have been proposed as green adsorbents for treatment of wastewater polluted by heavy metals [21], organic dyes [22], aromatic and linear hydrocarbons [23]. Some more, recent works have shown that magnetic materials, consisting of Fe^0 (zero valent iron, or ZVI) and/or iron oxide nanoparticles (typically magnetite and/or maghemite),

can be conjugated/encapsulated in a (bio)polymeric matrix for wastewater remediation processes [24-26]. Such hybrid materials may combine the advantages of both components (i.e. the magnetic core and the polymeric shell), which allow high efficiency and selectively for pollutant removal and easy separation of the materials from the aqueous media after use by applying an external magnetic field. It was also shown that carbon-encapsulated magnetic nanoparticles have received a great attention with respect to the polymeric and silica coated ones, due to higher chemical and thermal stability, biocompatibility, superior porosity and enhanced affinity toward hydrophobic substrates [27,28]. Also in this field many studies are investigating both the preparation and the testing of carbon and carbon-derived magnet-sensitive nanoparticles with promising results [29-32].

In this work, multifunctional nanoparticles, made of bio-derived adsorbent (chitosan) and magnet-responsive materials, have been produced through a co-precipitation reaction in a one-step procedure coupled to a pyrolysis treatment at 550°C and 800°C (i.e. before and after the iron oxides interphase conversion, *vide infra*) [25]. A deep physicochemical characterization of the chitosan-based magnetic materials were carried out and the sorption properties of these materials were tested in magnetically-guided water remediation experiments from selected PAHs. Interestingly, the hybrid character of the obtained materials (hydrophobic surface and magnetic properties), together with the precursor abundance, can make these materials suitable for sustainable and efficient wastewater purification processes from PAHs.

Experimental

Materials. Commercially available partially N-deacetylated chitosan (DD = 75–85%) of medium molecular weight (M_v = 190–310 kDa) with Brookfield viscosity of 200–800 cps (from crab shells, Aldrich) is selected as stabilizing/polymeric matrix. Iron oxide precursors are anhydrous ferric chloride $FeCl_3$ (purity ≥ 98%, Fluka Chemika) and ferrous sulfate heptahydrate $FeSO_4 \cdot 7H_2O$ (purity ≥ 99.5%, Fluka Chemika). Other reagents used are: ammonium hydroxide solution (NH_3 essay 28-30%, E. Merck), hydrochloric acid (HCl, 37 wt.%, Fluka Chemika). Naphthalene (NAP), acenaphthylene (ACL), acenaphthene (AC), fluorine (FL), phenanthrene (PHE), anthracene (ANT), fluoranthene (FN) and pyrene (PY) were purchased from Sigma-Aldrich (purity > 99.0%). All aqueous solutions for adsorption experiments were prepared using ultrapure water Millipore Milli-Q™. All chemicals were used without further purification.

Synthesis of chitosan- and chitosan-derived magnet-responsive materials. $FeCl_3$ (3.7 g) and $FeSO_4 \cdot 7H_2O$ (4.17 g) salts (with Fe(III)/Fe(II) molar ratio = 1.5) were dissolved in 100 mL of deionized water at RT and heated up to 90°C. As soon as the desired temperature was reached, two

other solutions were added in sequence: a) 10 mL of 25 %vol ammonium hydroxide, and b) 50 mL of a previously prepared chitosan aqueous solution in a weak acid environment (i.e. to favor the solubility of chitosan). In particular, three stock solutions having different content of chitosan (1, 2, and 3 %wt) were prepared by using HCl (2, 4, and 6 %vol, respectively). Mixtures have been stirred at 90°C for 30 min and then cooled to room temperature. The magnet-sensitive black viscous solutions were then purified by washing twice with deionized water and oven-dried at 80°C overnight. According to this procedure, dispersions of iron oxide particles in the chitosan matrix are expected to form [25]. The so-obtained materials (here called MC1, MC2 or MC3, depending on the chitosan quantity used in the synthesis: 1 %wt, 2 %wt or 3 %wt, respectively) were pyrolized in a quartz tube reactor by thermal treatments at 550°C or at 800°C for 1 h (heating rate: 5°C min^{-1}) under nitrogen flow (250 mL min^{-1}). Pyrolyzed materials were coded as MC1py550, MC2py550, MC3py550, MC1py800, MC2py800 or MC3py800, where the first number indicates the amount of chitosan and the second number represents the pyrolysis temperature. Finally, neat magnetite/maghemite (M0) was obtained from the previous procedure without chitosan addition and pyrolysis treatment.

Structure, surface and magnetic characterizations. X-ray diffraction (XRD) patterns were recorded by using an X'Pert PRO MPD diffractometer from PANalytical, equipped with Cu anode, working at 45 kV and 40 mA in a Bragg-Brentano geometry on a spinner sample-holder (60 rpm). The XRD pattern acquisition was performed with a 0.02° interval steps, 45 s $step^{-1}$ to improve the signal to noise ratio. Fourier transform infrared (FTIR) spectra were recorded by means of a Bruker Vector 22 spectrophotometer equipped with Globar source, DTGS detector, and working in transmission mode with 128 scans at 4 cm^{-1} resolution in the 4000-400 cm^{-1} range. Samples were previously dispersed in KBr (1:20 weight ratio). Potential magnetization measurements were carried out by using a LakeShore 7404 vibrating sample magnetometer and the hysteresis loop of all samples was registered at RT. The magnetic field was cycled between -20000 and 20000 Gauss. Scanning electron microscopy (SEM) analyses were performed by using a ZEISS EVO 50 XVP microscope with LaB_6 source, equipped with detector for secondary electrons. SEM measurements were performed on metal sputtered samples (gold film thickness of about 15 nm, Bal-tec SCD050 sputter coater). High-resolution transmission electron microscopy (HRTEM) was used to evaluate morphology and structure of the materials at a nanometric level. Micrographs were obtained using a JEOL JEM 3010 instrument (300 kV) equipped with a LaB_6 filament. For the specimen preparation, a few drops of NPs water suspensions were poured on holed carbon-coated copper grids and left to dry before analyses. Atomic force microscopy measurements were performed in the intermittent-

contact mode by using a modified Easyscan2 AFM instrument (Nanosurf), equipped with a 10 µm scan-head, high performance anti-vibration platform and a shielded (Faraday cage) and acoustically insulated enclosure. Magnetic force microscopy (MFM) imaging was performed by using the same instrumental setup in a dual-scan mode. The first scan was used for the morphological imaging, while the second scan was operated at constant-height (H) above the same surface with a commercial magnetic probe (Multi75M-G, Bud-get Sensors; resonant frequency = 75 kHz, force constant = 3 N m^{-1}) with a tip radius of about 60 nm by monitoring the phase and the amplitude shifting. The magnetic tip was magnetized by an external magnet (magnetization along the tip-sample axis) and tested on a magnetic grid prior to measurements.

Adsorption experiments of PAHs in water. PAHs adsorptions onto the prepared nanomaterials were determined by batch experiments in closed Pyrex-flasks (containing 200 mL solutions) under continuous stirring at 25°C. ANT and NAP were used as PAHs reference in independent experiments. Kinetic experiments were carried out by contacting 500 mg L^{-1} of the prepared nanomaterials with a solution containing 50 µg L^{-1} of ANT, and by sampling at fixed times up to a maximum of 24 h. Contacts were performed at circumneutral pH, which did not change during the experiment (data not shown for the sake of brevity). Equilibrium isotherm experiments were carried out adding 50 mg L^{-1} of nanomaterials to a solution with the initial probe (ANT or NAP) concentration ranging from 20 µg L^{-1} to 80 µg L^{-1} (contact time of 4 h at RT). After contact, an aliquot of 5 mL was withdrawn, the sorbent was magnetically separated from the solution and the PAHs were analyzed on the supernatant. All adsorption experiments were carried out in duplicate. The amount of PAHs sorbed at equilibrium (q_e, $\mu g\ g^{-1}$) was estimated as follows:

$$q_e = \frac{(C_0 - C_e) \times V}{m} \qquad \text{(Eq. 1)}$$

where C_0 and Ce (µg L^{-1}) are the initial and equilibrium liquid phase concentration of PAHs, respectively. V (L) is the solution volume, and m (g) is the mass of the sorbent.

Competitive adsorption experiments with a mixture of eight PAHs onto MC3py550 were also performed. The PAHs mixture, composed of NAP, ACL, AC, FL, PHE, ANT, FN and PY in ultrapure water, was prepared from a dilution of a PAHs mixture stock solutions (20 mg L^{-1} of each PAH in methanol) with ultrapure water and agitation during 48 h at RT in amber borosilicate glass containers. Final methanol concentrations were kept under 0.1% of the total solution volume to avoid co-solvent effects. The initial concentrations of each PAH ranged from 2.2 to 44 µg L^{-1}. In

sorption experiments with the PAHs mixture, 50 mg L^{-1} of adsorbent were used. The removal efficiency of each PAHs (*RE%*) was calculated as follows:

$$RE\% = \frac{(C_0 - C_e) \times 100}{C_0} \quad \text{(Eq. 2)}$$

Analysis of PAHs: Two instruments were used: a fluorescence spectrometer (F-7000 Hitachi) and a gas chromathograph mass spectrometer (GC-MS, Agilent 6890N GC and 5973 MSD). Each instrument was used to determine the final concentration of PAHs in sorption experiments. Fluorescence spectrometer was used for the analysis of ANT and NAP in the sorption kinetics and adsorption isotherm measurements. The excitation wavelengths were 250 nm (ANT) and 220 nm (NAP), whereas the fluorescence intensities were measured at 380 nm and 323 nm for ANT and NAP, respectively. Slit widths of excitation and emission were 2.5 nm and wavelength scan speed 240 nm min^{-1}. GC-MS was used for the analysis of each PAH in the sorption experiment with the mixture of PAHs, according to the procedures described in the literature [33-34]. Briefly: 200 mL of sample extracted after the magnetic separation was eluted through Strata® RP-18 cartridge; then PAHs were recovered with 6 mL of dichloromethane. The fraction was concentrated to 1 mL under a nitrogen stream, transferred to a glass vial and quantitated by gas-chromatography (GC-MS). A 30 m HP–5 MS fused silica column (0.25 mm i.d., 0.25 μm film thickness) was used. Column temperature: 38°C for 1 min, up to 300°C with ramping at 6 °C min^{-1} and held 5 min at 300°C. Samples were run in the electron impact mode at 70 eV and in the selected ion monitoring (SIM) mode with a 4.04 s scan time over a 50–450 amu range resolution. Each compound was recognized by a target ion and two qualifiers.

Results and discussion

Structure, morphology, and magnetic properties

The structure of the chitosan–based materials before and after the thermal treatments at 550°C and at 800°C, compared to the neat chitosan, has been investigated by means of XRD, FTIR and HRTEM analyses. Similar results among materials with the different chitosan %wt were obtained, thus, for the sake of brevity, only MC3-derived samples are discussed. XRD pattern (Figure 1 and inset therein) shows many reflections, including maxima at 2θ = 30.1°, 35.4°, 43.0°, 53.9°, 57.2° which can be associated with (220), (311), (400), (422), (511) X-ray diffraction planes of magnetite (card number 00-019-0629, ICCD Database) [19] and/or maghemite (card number 00-039-1346, ICCD Database) [25]. The two phases cannot be distinguished by means of XRD data,

but the presence of maghemite is supposed given the easy topotactic oxidation of magnetite into maghemite which is a well-known phenomenon already described in the literature (see [25] and references within). It is noteworthy that the signal at $2\theta = 33°$, which is associated with ammonium chloride (card number 01-073-0363, ICCD Database), disappears upon pyrolysis (C and D XRD patterns in Figure 1), thus indicating that the removal of byproducts is effective upon the adopted thermal treatments. In addition, from the XRD pattern of MC3Py800 (D pattern in Figure 1), the gradual disappearance of magnetite/maghemite is shown together with the formation of metallic iron (see labeled peaks with maxima at $2\theta = 44.7°$ and 65.2° associated with the (110) and (200) planes of Fe^0 (card number 01-087-0722, ICCD Database).

FTIR spectra of MC3, MC3Py550 and MC3Py800 are shown and compared with neat chitosan in Figure 2. The chitosan skeletal fingerprint (C-O and C-O-C stretching vibrational modes of glycosidic functional groups) between 1150 cm^{-1} and 900 cm^{-1} is evidenced in MC3 (Figure 2, curves B and E, green box) [18]. Furthermore, the chitosan signals at 1230-1400 cm^{-1} (C–N axial stretching and CH_3 symmetrical deformation) [18,19], are partially covered by an intense and narrow peak at ca. 1400 cm^{-1} (Figure 2, curve B, red box), observed in all modified chitosan samples (i.e. MC1, MC2 and MC3). Interestingly, the formation of this sharp peak could be plausible due to the interaction between chitosan O-containing polar groups and iron species [35,36]. The presence of modes at 575 and 620 cm^{-1}, due to Fe-O stretching vibrations confirms the formation of the iron oxide phase (Figures 2, curves A, B and C in blue box) [25]. To verify a possible N-deacetylation phenomenon involving chitosan, the biopolymer was treated following the NPs preparation procedure in hot-base-containing environment at 90°C without the presence of the iron-containing salts. FTIR data involving the amide functionalities of both neat and hot-base-treated chitosan are reported in Figure S1 (Supporting Information). Basing on the results obtained, it seems that no modifications in chitosan functionalities occurred after the treatment in the basic environment at high temperature. After thermal treatment at 550°C, the disappearance of all chitosan signals is shown with the formation of a very sharp signal at ca. 1600 cm^{-1} typical of graphite-like C=C stretching mode (Figure 2, curves C and D in violet box) which is attributed to the incipient formation of a carbon phase, although bands in the region commonly assigned to Fe-O stretching (550-700 cm^{-1}) are still present (Figure 2, curve C). After thermal treatment at 800°C (Figure 2 D), a significant depletion of signals due to C=C aromatic species and the disappearance of all signals due to iron oxide species were observed (Figure 2D). However, the relative intensities of signals associated to C-H aliphatic streaching vibration (2852 and 2923 cm^{-1}) increased with respect to the band of C=C stretching. The morphologies of MC3, MC3py550 and MC3py800, obtained from SEM images, are shown in Figure S2 (Supporting Information). All samples are in

the form of micro-agglomerates with sizes of 0.5-5 μm (Figures S2A,C,E), exposing an irregular and quite complex surface. At higher magnification, more evident aggregation of nanoparticles are shown (Figures S2B,D,F), but at the adopted resolution nothing more can be inferred at the nanometric scale.

HRTEM images of the three samples are reported in Figure 3. Section A reports the images of MC3 sample before pyrolysis at low and high magnification. The presence of an amorphous phase, probably organic, is visible in the inset together with crystalline circular optically dense particles and crystalline acicular particles. The analysis of the fringe patterns of the latter dark particles does not allow to distinguish magnetite (Fe_3O_4) and maghemite (γ-Fe_2O_3) phases (it is evidenced the pattern relative to (316) plane of both phases), whereas the less dark sections show the reflection of (102) plane of chitosan (card number 00-039-1894, ICCD Database). Analogous behaviors are shown by MC3py550 sample whose image is reported in section B: also in this case the fringe pattern corresponding to (316) plane of magnetite/maghemite phase is visible whereas the amorphous phase covers the entire sample and it is never possible to observe patterns due to the presence of residual chitosan.

Completely different is the aspect of sample MC3py800 reported in section C. In general the sample shows amorphous parts together with crystalline moieties of different shapes: the pattern of (222) plane of magnetite and that of (110) plane of maghemite are evident in the amorphous framework. In addition zero valent iron Fe^0 ((211) plane pattern) and wüstite FeO ((111) plane pattern, card number 01-079-1968, ICCD Database) nanorods appear several time in the micropraphs. A prismatic shape is expected for wüstite, not so common for Fe^0, nevertheless the same shape can be shown by the two phases when wustite is transformed into Fe^0 during the pyrolysis process. The presence of these crystalline phases allows to confirm the reaction cycle expected for MC3 during the thermal treatment under the inert (reducing) environment. In fact, magnetite or maghemite in the presence of a carbon source (like chitosan) treated at temperature as high as 575°C in nitrogen atmosphere reduce into wüstite phase (FeO). In turn, FeO disproportionates giving Fe^0 and magnetite phases [25].

An extensive magnetic characterization has been performed and the results are summarized in Table S1 (Supporting Information). Furthermore, the magnetization curves of MC3, MC3Py550 and MC3Py800 are compared with that of neat magnetite/maghemite used as a reference in Figure 4. All samples exhibit superparamagnetic behaviors (i.e. very narrow hysteresis loop), with almost zero remanence (Mr) and low coercitivity ($Hc \leq 10$ G). The saturation magnetization (Ms) of chitosan-stabilized materials were 39 (MC1), 13 (MC2), and 12 (MC3) emu g^{-1}. Analogously to our previous work, this trend indicates a different amount of iron oxide per gram of sample (i.e.

different chitosan coverage) [25]. Additionally, the decrease in Ms for all the samples compared to the reference M0 (64 emu g^{-1}) is mainly due to the presence of not-magnet-sensitive species, such as the organic coating. In fact, the presence of the polymeric matrix surrounding the magnetic NPs reduces the magnetic moments in such NPs due to quenching of surface moments [24]. However, even though there is a significant decrease of the Ms values for chitosan-stabilized materials, all samples can be easily separated in few minutes by applying a permanent magnet and dried materials are magnetically-stable due to the chitosan protective matrix (Figure S3, Supporting Information). The pyrolysis treatment at 550°C mainly affects both remanence (Mr moves to values higher than 4.5 emu g^{-1}) and coercitivity ($78 \leq Hc \leq 111$ G). Curiously, among MCpy550 samples, MC1py550 registered a slight reduction of saturation magnetization (from 39 to 30 emu g^{-1}), whereas the Ms values for both MC2py550 and MC3py550 increased noticeably (from 13 up to 24 emu g^{-1} for MC2py550 and from 12 to 40 emu g^{-1} for MC3py550). Conversely, due to the pyrolysis treatment at 800°C, the Ms values of both MC2py800 and MC3py800 registered a remarkable increase, reaching respectively 138 emu g^{-1} and 93 emu g^{-1}. Both remanence and coercitivity were still higher than those of non-thermally treated materials, although they were significantly lower than those of samples treated at 550°C. The only exception is again sample MC1py800, which presents opposite trend (i.e. lower saturation and higher coercitivity). The higher values in terms of saturation, remanence and coercitivity for thermally treated samples confirm the formation of new magnet-sensitive phases. In fact, magnetite/maghemite react, as discussed above, to form Fe^0, which presents a different magnetism (ferromagnetism instead of magnetite ferrimagnetism) with a large saturation magnetization, and this is also reflected by the different magnetization curve profiles reported in Figure 4.

Due to the peculiar surface, magnetic and sorption properties (*vide infra*), only magnet-responsive chitosan treated at 550°C was selected for more accurate topographic and magnetic characterizations, by means of AFM and MFM analyses as shown in Figure 5. After dispersion/sonication in water (2 mg mL^{-1}), magnetic nanoparticles were separated by a permanent magnet, deposited on a freshly cleaved mica and AFM imaged (Figures 5A and 5B). Sizes, comprised in the 22-30 nm, have been obtained from height profiles of selected lines. On the other hand, phase shift in the lift mode scan to analyze the magnetic interactions in a second tapping/lift mode was used at different heights (H= 90 nm, 100 nm, 110 nm, 120 nm) to minimize topographic effects. Furthermore, to avoid response variations all images have been acquired by using the same tip probe. Negative phase shifting (darker regions in Figure 5C), typically associated with the attractive interactions between the tip and the sample [37], was observed in combination with a positive shift of the amplitude signal (Figure S4, Supporting Information). It is worth noticing that

the phase shifting gives a higher signal-to-noise ratio, and more interestingly, the reverse contrast observed between phase and amplitude images has been recognized for magnetic interactions [38]. Notice that the phase image contrast is highly influenced by the lift height as well documented in the literature.

PAHs adsorption properties

Preliminary experiments were performed in order to evaluate the potential application of such chitosan- and chitosan-derived stabilized magnet-sensitive materials in the adsorption of anthracene (ANT) and naphthalene (NAP) used as PAH references at circumneutral pH. The optimization of the experimental testing was carried out toward ANT, whereas adsorption isotherms at optimized conditions were performed toward both ANT and NAP. As reported in Figure 6A, the kinetic of adsorption of ANT (50 µg L^{-1}) toward the MC3-series (500 mg L^{-1}) depends on the preparation condition of adsorbent materials. In particular, MC3 material is not a good adsorbent for apolar substrate (ca. 26 µg L^{-1} residual ANT, 48% of removal after 22 hours of contact). In analogy to our previous study [25], the possible explanation of this behavior is due to the presence of chitosan polar functionalities (as also evidenced by FTIR spectra in Figure 2). Otherwise, pyrolysis treatments drastically change the adsorption capacity. In fact, after pyrolysis performed at 550°C and 800°C, the adsorption performance increases (both MC3py550 and MC3py800 registered a significant removal of ANT from the aqueous environment after only 4 h of contact, leaving in both cases residual ANT minor than ca. 2 µg L^{-1} corresponding to 96% or removal). This behavior is due to the increased hydrophobicity of the material after pyrolysis (i.e. loss of polar functionalities) and consequent formation of graphite-like structures. In fact, it is known that aromatic π systems, as graphite-like materials, where the fused aromatic rings may behave as both π-donors and –acceptors [39], can be engaged in π–π electron-donor-acceptor (EDA) interactions with a series of π-donors (e.g. benzene, toluene, PAHs) [40]. Figure 6B shows the effect of the chitosan loading used in the adsorbent synthesis on the removal of ANT after 4 h of contact time. Based on the obtained results, it seems that the higher the chitosan loaded, the higher the efficiency in terms of ANT recovery. Additionally, the results clearly confirmed that the samples not thermally treated are not good adsorbents for the removal of apolar substrates. Furthermore, the best adsorption behaviours are shown by magnetic chitosan systems pyrolyzed at 550°C, while MCpy800 samples show different behaviors depending on the amount of the initially loaded chitosan. This trend could be explained again considering the reaction cycle already mentioned [25]. The high structural inhomogeneity of pyrolysed systems could be responsible for the wider error bar characterizing the adsorption experiments on MC2py800 sample. The best performances were obtained for all MCpy550 samples

and for MC3py800 one, for this reason these samples were tested in the following experiments. In order to optimize the experimental conditions, and in particular to find out the minimum amount of adsorbent needed for an effective PAHs removal, several trials were performed by varying the adsorbents amount (25-500 mg L^{-1}). Data reported in Figure 6C show the residual ANT concentration after 4 h of contact with MC3py550 and MC3py800. The best performance was obtained for MC3py550. Additionally, the same experiments were also performed at different pH values (3, 6 and 9 with 25 mg L^{-1} of MC3py550 and 50 µg L^{-1} of ANT) and negligible variations were registered (data not reported for brevity). The equilibrium isotherms were performed for both ANT and NAP as substrates on MC3py550 (50 mg L^{-1}) at RT and circumneutral pH (Figure 5D). Adsorption isotherms were fit by the Freundlich model, $q_e = K_F C_e^n$, where n is the Freundlich exponent, which represents the linearity of a sorption isotherm, and K_F (mg^{1-n} L^n g^{-1}) is the Freundlich adsorption coefficient. The parameters were obtained by non-linear least-squares regression weighted by the dependent variable. Both ANT and NAP adsorptions on MC3py550 were almost linear in the range of concentrations studied, giving a Freundlich coefficient (n) of 1.08 and 1.10 and K_F of 10.95 and 9.53 for ANT and NAP, respectively. These values are consistent with those previously reported for other systems: carbon-based and magnetic permanently confined micelle array sorbents [41,42].mesoporous organosilica [43], and mesoporous micelle silica hybrid materials [44], whose application gaveK_F of 1.98, 0.28, 1.28. These K_F values are significantly lower than those obtained in this study using MC3py550, indicating a superior performance of MC3py550 in PAHs removal efficiency

To assess the affinity of MC3py550 towards different PAHs (i.e. the removal capacity), a mixture of NAP, ACL, AC, FL, PHE, ANT, FN and PY was contacted with 50 mg L^{-1} of adsorbent (Figure 7). The results showed different removal capacities depending on the structure of PAHs, in particular, high % removal (> 80%) was obtained for FL, ANT, PHE, PY and FN, whereas almost no retention was observed for NAP. The removal capacity increased together with the number of aromatic rings in the polycyclic structure, which increases the π-π interactions. This trend was reported for sorption of PAHs on carbon nanotubes and multiwalled carbon nanotubes [45]. On the other hand, although the isothermal adsorption tests using individual PAHs (Figure 6C) showed a significant q_e value for NAP, the low removal capacity observed in the PAHs mixture could be accounted for the competition among the PAHs for the active sites on the surface of MC3Py550.

Moreover, a clear trend of the removal capacity with the PAHs hydrophobicity (K_{ow}) was also observed (Figure 7). PAH molecules with higher hydrophobicity and more aromatic rings had stronger sorption affinity. This could also explain the low % removal of NAP, since it is the least hydrophobic PAH of the mixture ($\log K_{ow}$ = 3.37). Experimental evidences confirmed that the PAHs

sorption occurs following two mechanisms: in the first one the hydrophobicity of the material attracts PAHs to the adsorbing surface and in the second one the π–π interactions allow the adsorption of the molecules with the more extended aromaticity.

The obtained results along with the magnetic properties showed by these materials, clearly demonstrate that chitosan-derived iron oxide systems can be used as an efficient, versatile and low cost adsorbent for removing PAHs from wastewaters.

Acknowledgements

This work was realized with the financial support for academic interchange by the Marie Sklodowska-Curie Research and Innovation Staff Exchange project funded by the European Commission H2020-MSCA-RISE-2014 within the framework of the research project Mat4treaT (Project number:645551). Compagnia di San Paolo and University of Torino are gratefully acknowledged for funding Project Torino_call2014_L2_126 through ‘‘Bando per il finanziamento di progetti di ricerca di Ateneo – anno 2014’’ (Project acronym: Microbusters). Additionally, authors would like to acknowledge Dr. Flavio R. Sives (La Plata, Argentina) for magnetization measurements and Dr. Maria Carmen Valsania (Torino, Italy) for TEM measurements.

Supporting information

Figures S1−S4 and Table S1.

References

[1] Mercogliano, R.; Santonicola, S.; De Felice, A.; Anastasio, A.; Murru, N.; Ferrante, M.C.; Cortesia, M.L. Occurrence and distribution of polycyclic aromatic hydrocarbons in mussels from the gulf of Naples, Tyrrhenian Sea, Italy. *Marine Poll. Bull.* **2016**, 104, 386-390.

[2] Hijosa-Valsero, M.; Bécares, E.; Fernández-Aláez, C.; Fernández-Aláez, M.; Mayo, R.; Jiménez, J.J. Chemical pollution in inland shallow lakes in the Mediterranean region (NW Spain): PAHs, insecticides and herbicides in water and sediments. *Sci. Total Environ.* **2016**, 544, 797-810.

[3] Sarria-Villa, R.; Ocampo-Duque, W.; Páez, M.; Schuhmacher, M. Presence of PAHs in water and sediments of the Colombian Cauca River during heavy rain episodes, and implications for risk assessment. *Sci.Total Environ.* **2016**, 540, 455-465.

[4] Ivshina, I.B.; Kuyukina, M.S.; Krivoruchko, A.V.; Elkin, A.A.; Makarov, S.O.; Cunningham, C.J.; Peshkur, T.A.; Atlas, R.M.; Philp, J.C. Oil spill problems and sustainable response strategies through new technologies. *Environ. Sci.: Processes Impacts* **2015**, 17, 1201-1219.

[5] Pontevedra-Pombal, X.; Rey-Salgueiro, L.; García-Falcón, M. S.; Martínez-Carballo, E.; Simal-Gándara, J.; Martínez-Cortizas, A., Pre-industrial accumulation of anthropogenic polycyclic aromatic hydrocarbons found in a blanket bog of the Iberian Peninsula. *Environ. Res.* **2012**, 116, 36-43.

[6] Office of the Federal Registration (OFR) Appendix A: priority pollutants. Fed Reg. 1982, 47, 52309.

[7] Choi, H.M.; Cloud, R.M. Natural sorbents in oil spill cleanup. *Environ. Sci. Technol.* **1992**, 26, 772-776.

[8] Lessard, R.R.; Demarco, G. The significance of oil spill dispersants. *Spill Sci. Technol. Bull.* **2000**, 6, 59-68.

[9] Dave, D.; Ghaly, A.E. Remediation technologies for marine oil spills: A critical review and comparative analysis. *Am. J. Environ. Sci.* **2011**, 7 (5), 423-440.

[10] Nordvik, A.B. Time window-of-opportunity strategies for oil spill planning and response. *Pure Appl. Chem.* **1999**, 71, 5-16.

[11] Ornitz, B.E.; Champ, M.A., *Oil Spills First Principles: Prevention and Best Response*; Elsevier Science Ltd, Press: Amsterdam, 2002.

[12] Cravanzola, S.; Jain, S.; Cesano, F.; Damin, A.; Scarano, D. Development of a multifunctional TiO_2/MWCNT hybrid composite grafted on a stainless steel grating. *RSC Adv.* **2015**, 5, 103255-103264.

[13] Teas, C.; Kalligeros, S.; Zanikos, F.E.; Stournas, S.; Lois, E.; Anastopoulos, G. Investigation of the effectiveness of absorbent materials in oil spills clean up. *Desalination* **2001**, 140, 259-264.

[14] Pérez-Gregorio, M. R.; García-Falcón, M. S.; Martínez-Carballo, E.; Simal-Gándara, J., Removal of polycyclic aromatic hydrocarbons from organic solvents by ashes wastes. *J. Hazard. Mater.* **2010**, 178 (1–3), 273-281.

[15] Hajji, S.; Younes, I.; Ghorbel-Bellaaj, O.; Hajji, R.; Rinaudo, M.; Nasri, M; Jellouli, K. Structural differences between chitin and chitosan extracted from three different marine sources. *Int. J. Biol. Macromol.* **2014**, 65, 298–306.

[16] Al Sagheer, F.A.; Al-Sughayer, M.A.; Muslim, S.; Elsabee, M.Z. Extraction and characterization of chitin and chitosan from marine sources in Arabian Gulf. *Carbohyd. Polym.* **2009**, 77 (2), 410-419.

[17] Kerton, F.M.; Liu, Y.; Omari, K.W.; Hawboldt, K. Green chemistry and the ocean-based biorefinery. *Green Chem.* **2013**, 15, 860-871.

[18] Corazzari, I.; Nisticò, R.; Turci, F.; Faga, M.G.; Franzoso, F.; Tabasso, S.; Magnacca, G. Advanced physico-chemical characterization of chitosan by means of TGA coupled on-line with

FTIR and GCMS: Thermal degradation and water adsorption capacity. *Polym. Degrad. Stabil.* **2015**, 112, 1-9.

[19] Nisticò, R.; Faga, M.G.; Gautier, G.; Magnacca, G.; D'Angelo, D.; Ciancio, E.; Piacenza, G.; Lamberti, R.; Martorana, S. Physico-chemical characterization of functionalized polypropylenic fibers for prosthetic applications. *Appl. Surf. Sci.* **2012**, 258, 7889-7896.

[20] Avetta, P.; Nisticò, R.; Faga, M.G.; D'Angelo, D.; Aimo Boot, E.; Lamberti, R.; Martorana, S.; Calza, P.; Fabbri, D.; Magnacca, G. Hernia-repair prosthetic devices functionalised with chitosan and ciprofloxacin coating: Controlled release and antibacterial activity. *J. Mater. Chem. B* **2014**, 2, 5287-5294.

[21] Vijaya, Y.; Popuri, S.R.; Boddu, V.M.; Krishnaiah, A. Modified chitosan and calcium alginate biopolymer sorbents for removal of nickel (II) through adsorption. *Carboh. Polym.* **2008**, 72, 261-271.

[22] Wan Ngah, W.S.; Teong, L.C.; Hanafiah, M.A.K.M. Adsorption of dyes and heavy metal ions by chitosan composites: A review. *Carboh. Polym.* **2011**, 83, 1446-1456.

[23] Crisafully, R.; Milhome, M.A.L.; Cavalcante, R.M.; Silveira, E.R.; De Keukeleire, D.; Nascimento, R.F. Removal of some polycyclicaromatic hydrocarbons from petrochemical wastewater using low-cost adsorbents of natural origin. *Bioresource Techn.* **2008**, 99, 4515-4519.

[24] Magnacca, G.; Allera, A.; Montoneri, E.; Celi, L.; Benito, D.E.; Gagliardi, L.G.; González, M.C.; Mártire, D.O.; Carlos, L. Novel magnetite nanoparticles coated with waste-sourced biobased substances as sustainable and renewable adsorbing materials. *ACS Sustainable Chem. Eng.* **2014**, 2,1518-1524.

[25] Cesano, F.; Fenoglio, G.; Carlos, L.; Nisticò, R. One-step synthesis of magnetic chitosan polymer composite films. *Appl. Surf. Sci.* **2015**, 345, 175-181.

[26] Li, Y.; Yuan, D.; Dong, M.; Chai, Z.; Fu, G. Facile and green synthesis of core-shell structured magnetic chitosan submicrospheres and their surface functionalization. *Langmuir* **2013**, 29, 11770-11778.

[27] Lu, A.H.; Salabas, E.L.; Schüth, F. Magnetic nanoparticles: Synthesis, protection, functionalization, and application. *Angew. Chem. Int. Ed.* **2007**, 46, 1222-1244.

[28] Cesano, F.; Rahman, M.; Bardelli, F.; Damin, A.; Scarano, D. Magnetic hybrid carbon via graphitization of polystyrene-co-divinylbenzene: morphology, structure and adsorption properties. *ChemistrySelect* **2016**, 1, 2536-2541.

[29] Zhu, Q.; Tao, F.; Pan, Q. Fast and selective removal of oils from water surface via highly hydrophobic core-shell Fe_2O_3@C nanoparticles under magnetic field. *ACS Appl. Mater. Interfaces* **2010**, 2 (11), 3141-3146.

[30] Gui, X. Zeng, Z.; Lin, Z.; Gan, Q.; Xiang, R.; Zhu, Y.; Cao, A.; Tang, Z. Magnetic and highly recyclable macroporous carbon nanotubes for spilled oil sorption and separation. *ACS Appl. Mater. Interfaces* **2013**, 5 (12), 5845-5850.

[31] Gupta, S.; Tai, N.H. Carbon materials as oil sorbents: A review on the synthesis and performance. *J. Mater. Chem. A* **2016**, 4, 1550-1565.

[32] Chu, Y.; Pan, Q. Three-dimensionally macroporous Fe/C nanocomposites as highly selective oil-absorption materials. *ACS App. Mater. Interfaces* **2012**, 4 (5), 2420–2425.

[33] García-Falcon, M.S.; Peréz-Lamela, M.; Simal-Gándara, J. Comparison of strategies for extraction of high molecular weight polycyclic aromatic hydrocarbons from drinking waters. *J. Agric. Food Chem*. **2004**, 52 (23), 6897-6903.

[34] Peng, C.; Chen, W.; Liao, X.; Wang, M.; Ouyang, Z.; Jiao, W.; Bai, Y. Polycyclic aromatic hydrocarbons in urban soils of Beijing: Status, sources, distribution and potential risk. *Environ. Pollut*. **2011**, 159, 802-808.

[35] Safari, J.; Javadian, L. Chitosan decorated Fe_3O_4 nanoparticles as a magnetic catalyst in the synthesis of phenytoin derivatives. *RSC Adv.* **2014**, 4, 48973-48979.

[36] Salehizadeh, H.; Hekmatian, E.; Sadeghi, M.; Kennedy, K. Synthesis and characterization of core-shell Fe_3O_4-gold-chitosan nanostructure. *J. Nanobiotechnology* **2012**, 10:3.

[37] Mohamed, H.D.A.; Watson, S.M.D.; Horrocks, B.R.; Houlton, A. Magnetic and conductive magnetite nanowires by DNA-templating. *Nanoscale* **2012**, 4, 5936–5945.

[38] Li, H.; Qi, X.; Wu, J.; Zeng, Z.; Wei, J.; Zhang, H. Investigation of MoS_2 and graphene nanosheets by magnetic force microscopy. *ACS Nano* **2013**, 7, 2842-2849.

[39] Keiluweit, M.; Kleber, M. Molecular-Level Interactions in Soils and Sediments: The Role of Aromatic π-Systems. *Environ. Sci. Technol.* **2009**, 43, 3421-3429.

[40] Zhu, D.; Pignatello, J. J. Characterization of Aromatic Compound Sorptive Interactions with Black Carbon (Charcoal) Assisted by Graphite as a Model. *Environ. Sci. Technol.* **2005**, 39, 2033-2041.

[41] Clark, K. K.; Keller, A. A. Investigation of two magnetic permanently confined micelle array sorbents using nonionic and cationic surfactants for the removal of PAHs and pesticides from aqueous media. *Water, Air, Soil Pollut.* **2012**, 223, 3647-3655.

[42] Boving, T. B.; Zhang, W. Removal of aqueous-phase polynuclear aromatic hydrocarbons using aspen wood fibers. *Chemosphere* **2004**, 54, 831-839.

[43] Vidal, C. B.; Barros, A. L.; Moura, C. P.; de Lima, A. C. A.; Dias, F. S.; Vasconcellos, L. C. G.; Fechine, P. B. A.; Nascimento, R. F. Adsorption of polycyclic aromatic hydrocarbons from

aqueous solutions by modified periodic mesoporous organosilica. *J. Colloid Interface Sci.* **2011**, 357, 466-473.

[44] Shi, Y.; Li, B.; Wang, P.; Dua, R.; Zhao, D. Micelle swelling agent derived cavities for increasing hydrophobic organic compound removal efficiency by mesoporous micelle@silica hybrid materials. *Microporous Mesoporous Mater*. **2012**, 155, 252-257.

[45] Kragulj, M.; Tričković, J.; Dalmacija, B.; Kukovecz, Á.; Kónya, Z.; Molnar, J.; Rončević, S. Molecular interactions between organic compounds and functionally modified multiwalled carbon nanotubes. *Chem. Eng. J*. **2013**, 225, 144-152.

Figures

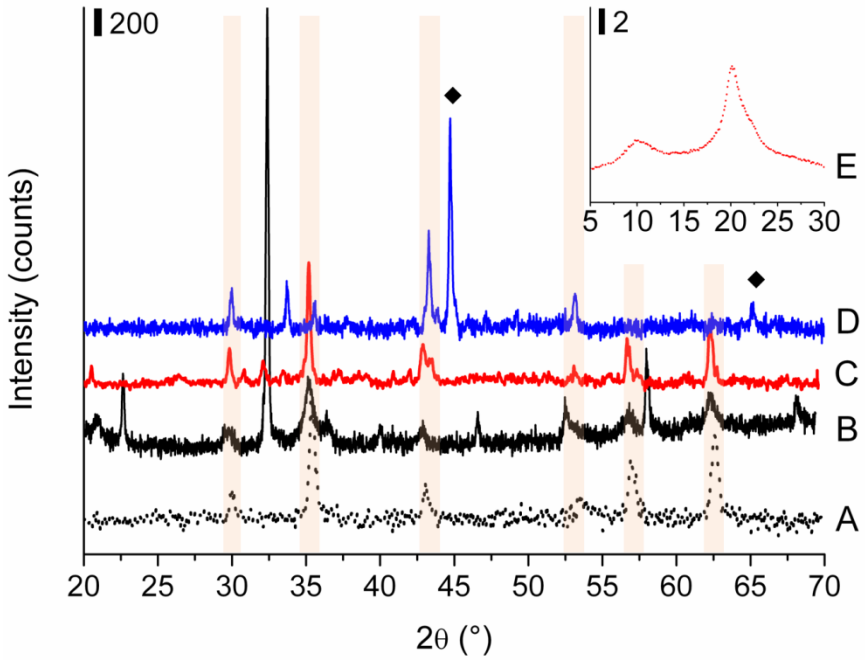

Figure 1. XRD patterns of MC3 (B, black solid curve), MC3py550 (C, red solid curve), and MC3py800 (D, blue solid curve) compared to the neat chitosan (red dotted curve E, inset) and magnetite/maghemite M0 (A, black dotted curve). Main reflections due to magnetite are highlighted (colored background). Black diamonds refer to the pyrolysis product Fe^0, whereas not-labeled peaks refer to by-products signals.

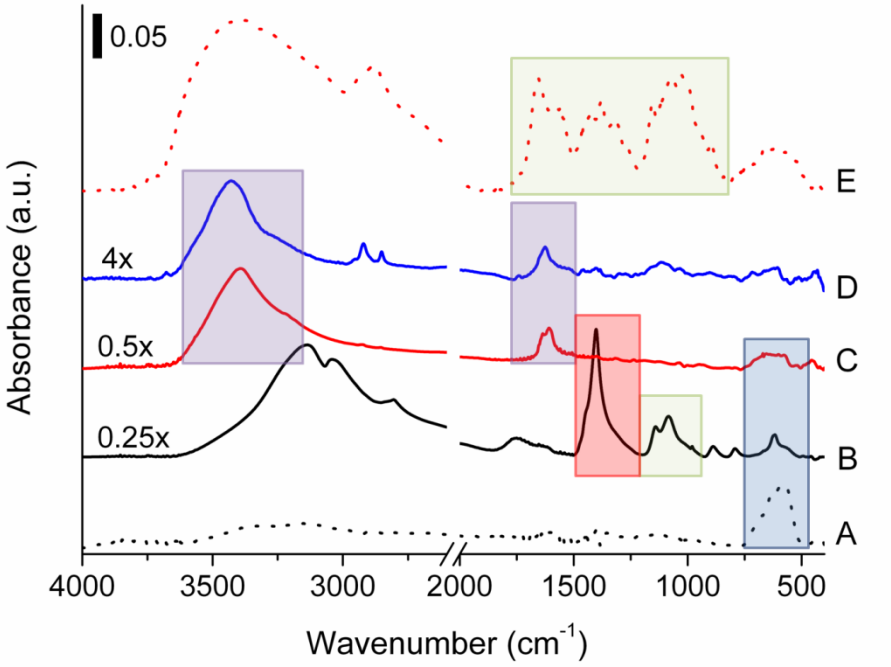

Figure 2. Absorbance FTIR spectra of MC3 (B, black solid curve), MC3Py550 (C, red solid curve), and MC3Py800 (D, blue solid curve), as compared to neat magnetite/maghemite M0 (A, black dotted curve), and neat chitosan (E, red dotted curve).

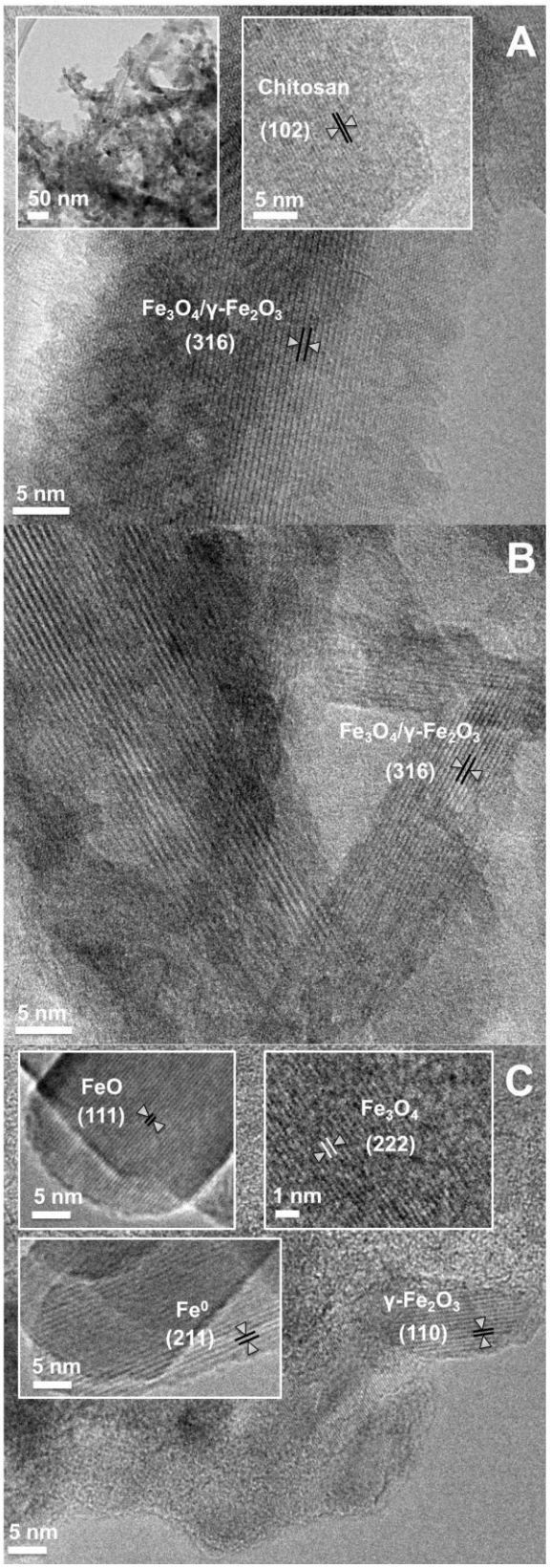

Figure 3. HRTEM micrographs of MC3 (A), MC3py550 (B), and MC3py800 (C). Inset in panel A refers to MC3 collected at low magnification, whereas insets in panel C refer to the presence of different iron-containing phases. Phases and crystalline planes are highlighted in each figure.

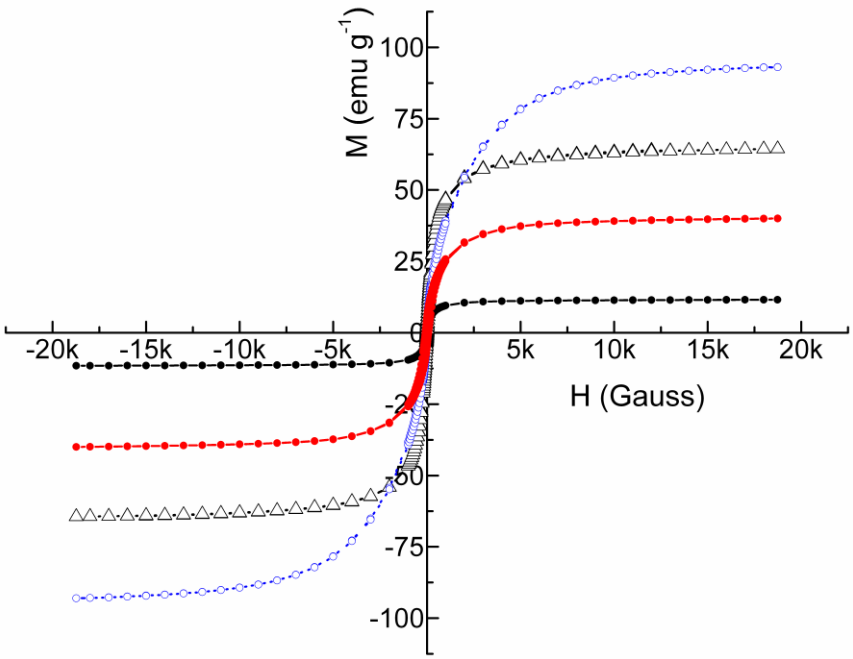

Figure 4. Magnetization curves of MC3 (black circles, black solid curve), MC3py550 (red circles, red solid curve), and MC3py800 (white circles, blue dotted curve) as compared to neat magnetite/maghemite M0 (white triangles, black dotted curve).

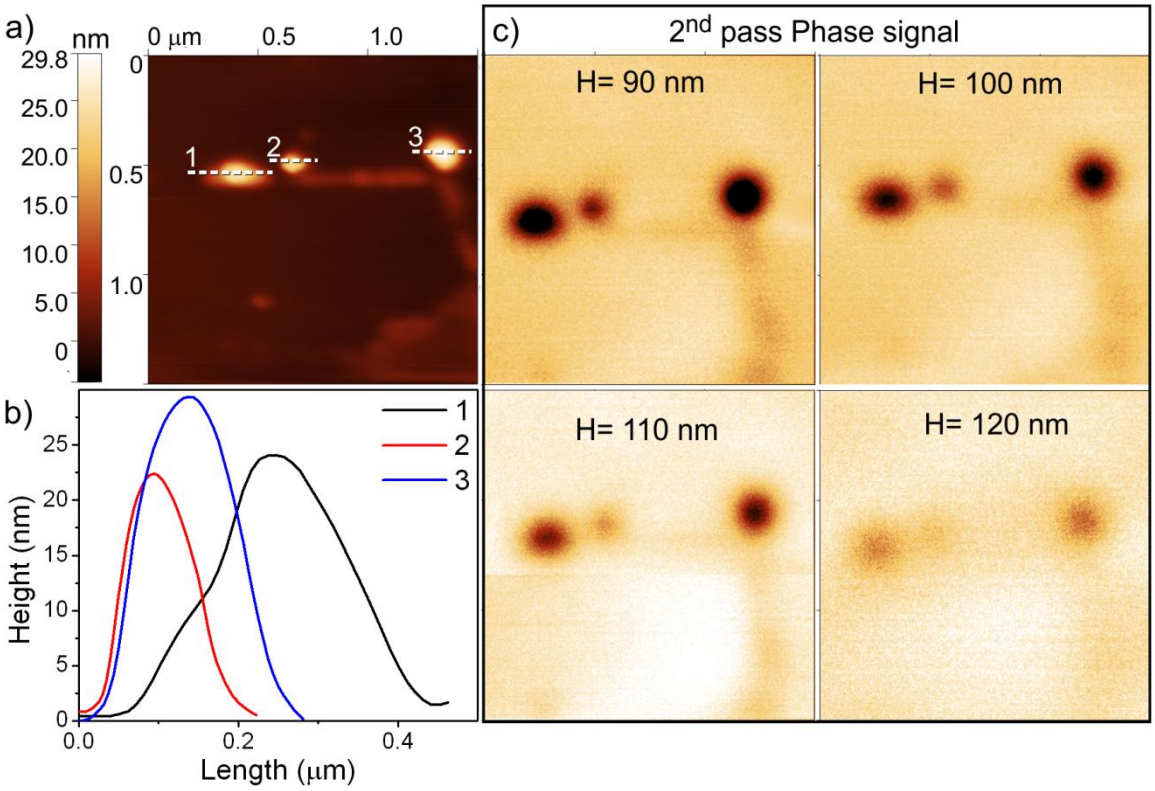

Figure 5. MC3py550AFM topography (A), height profiles (B), MFM phase images of the region (C) obtained at various lift heights (H = 90 nm, 100 nm, 110 nm and 120 nm).

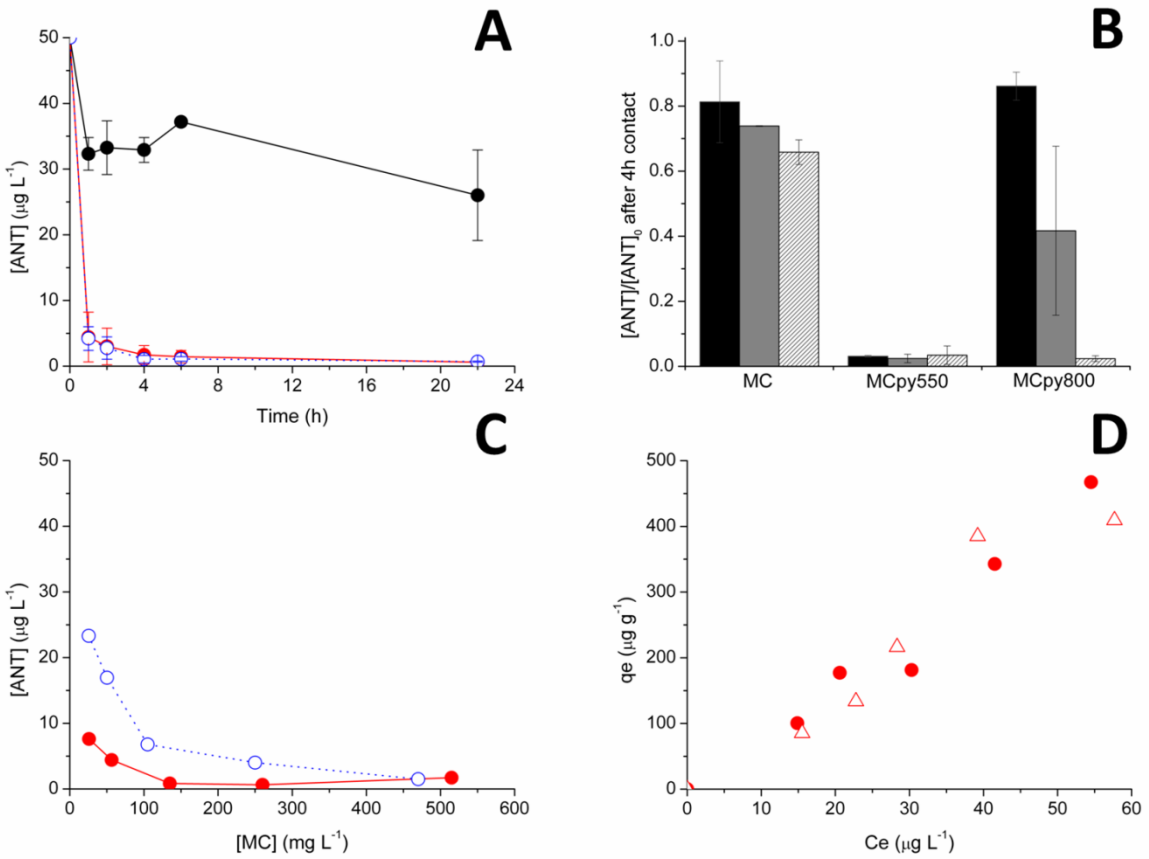

Figure 6. Adsorption experiments toward ANT and NAP. (A) Kinetics of adsorption ANT on MC3 (black circles, black solid line), MC3py550 (red circles, red solid line), and MC3py800 (white circles, blue dotted line). [ANT] = 50 µg L^{-1}, [sorbent] = 500 mg L^{-1}. (B) ANT removal obtained with MC1-series (black histograms), MC2-series (grey histograms), and MC3-series (obliquely-striped white histograms). [ANT] = 50 µg L^{-1}, [sorbent] = 500 mg L^{-1}, contact time = 4 hours. (C) Effect of sorbent concentration on the adsorption of ANT. MC3py550 (red circles, red solid line), and MC3py800 (white circles, blue dotted line). [ANT] = 50 µg L^{-1}, contact time = 4 h. (D) Adsorption isotherms of ANT (red circles) and NAP (white triangles) on MC3py550. [MC3py550] = 50 mg L^{-1}, contact time = 4 h). All experiments are performed at both RT and circumneutral pH.

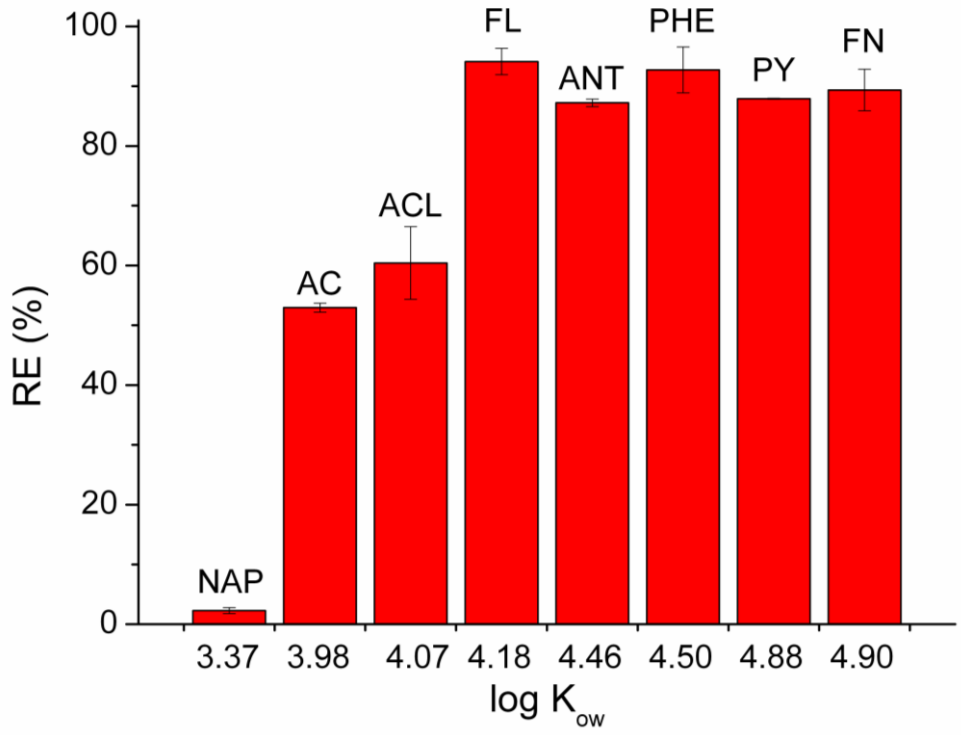

Figure 7. Adsorption experiments of a mixture of PAHs on MC3py550. [PAHs] = 2.2 to 44 µg L^{-1}, [MC3py550] = 50 mg L^{-1}, contact time = 24 h, RT and circumneutral pH.